SUPPLEMENTARY INFORMATION

One-pot spray pyrolysis method for nanostructured cobalt sulfide-C composite microspheres using recovered cobalt sulfuric acid solution and their excellent properties as anode materials for potassium-ion batteries

Yeong Beom Kim,‡[ac] A Yeon Jo,‡[a] Seulgi Kim,[b] Seungo Jeong,[b] Yun Chan Kang,*[c] Dongju Lee,*[ab] and Gi Dae Park*[ab]

[a]*Department of Advanced Materials Engineering, Chungbuk National University, Chungdae-ro 1, Seowon-Gu, Cheongju, Chungbuk 28644, Republic of Korea, E-mail: gdpark@chungbuk.ac.kr; dongjulee@chungbuk.ac.kr*

[b]*Department of Urban, Energy, and Environmental Engineering, Chungbuk National University, Chungdae-ro 1, Seowon-Gu, Cheongju, Chungbuk 28644, Republic of Korea*

[c]*Department of Materials Science and Engineering, Korea University, Anam-Dong, Seongbuk-Gu, Seoul 136-713, Republic of Korea, E-mail: yckang@korea.ac.kr*

‡ These authors contributed equally to this work.

Materials Characterizations

The morphological characteristics of the samples were investigated via scanning electron microscopy (SEM, VEGA3) and field emission-transmission electron microscopy (FE-TEM, JEM-2100F) at the Korea Basic Science Institute (Daegu). The crystal structures of the samples were analyzed using X-ray diffraction (XRD, PANalytical/Empyrean with Cu K_α radiation, λ = 1.5418 Å) at the Korea Basic Science Institute (Daedeok Headquarters). The Rietveld refinement of obtained XRD data was carried out using the FULLPROF software. X-ray photoelectron spectroscopy (XPS) of the samples was performed using ESCALAB-250 with Al K_α radiation (1486.6 eV). Thermogravimetric (TG) analysis (Pyris 1 Thermogravimetric Analyzer, PerkinElmer) was conducted in the range 25–800 °C at 10 °C min^{-1} under an air atmosphere. The carbon and sulfur contents in the samples were determined by elemental analyzer instrument (EA, Vario MICRO cube). The structural characteristics of carbon in the sample were investigated via Raman spectroscopy (Jobin Yvon LabRam HR800, excited by a 632.8-nm He/Ne laser) at room temperature.

Electrochemical Measurements

To measure the electrochemical properties of the samples for KIBs, a 2032-type coin cell constructed from electrodes prepared via the slurry process was utilized. For the anode electrode, the active materials, carbon black (Super-P), and sodium carboxymethyl cellulose (CMC) in a weight ratio of 7:2:1 were uniformly mixed with water solvent in a mortar. The well-mixed slurry was coated onto Cu foil using a doctor blade and dried in a vacuum oven for 3 h. Potassium metal and a microporous polypropylene film were used as the counter electrode and separator, respectively. The electrolyte for KIBs was 3 M potassium bis(fluoroslufony)imide (KFSI) dissolved in 1,2-dimethoxyethane (DME). The diameter and mass loading of the negative electrode were 14 mm and 1.4 mg cm^{-2}, respectively. The discharge–charge characteristics of the samples were analyzed via cycling in 0.001–3.0 V potential range at various current densities. Cyclic voltammetry (CV) analysis was conducted at a scan rate of 0.1 mV s^{-1}. Electrochemical impedance spectroscopy (EIS, ZIVE SP1) measurements of the electrode were performed over a frequency range of 0.01 Hz – 100 kHz. In-situ EIS analysis was performed at preselected potentials during the discharge and charge process at a current density of 0.1 A g^{-1}.

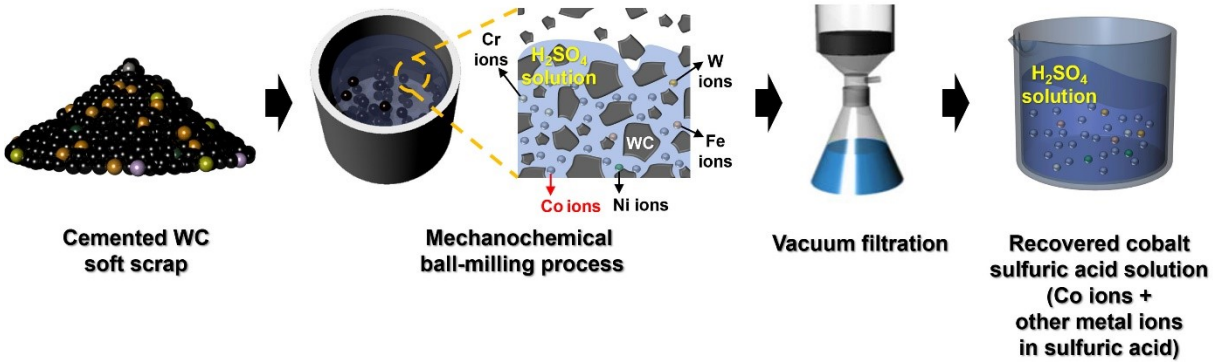

Fig. S1 Schematic illustration of cobalt recycling process from cemented WC soft scrap through mechanochemical ball-milling process.

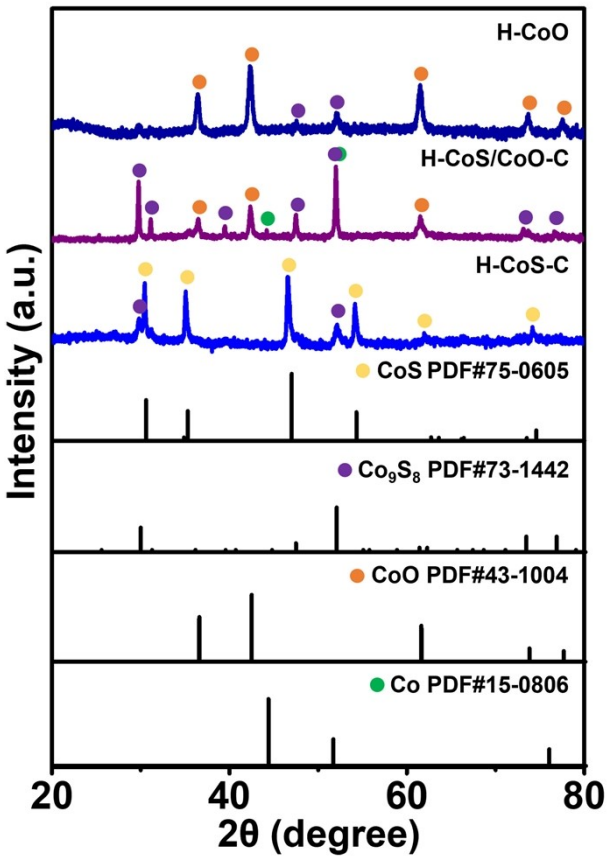

Fig. S2 XRD patterns of H-CoO, H-CoS/CoO-C, and H-CoS-C.

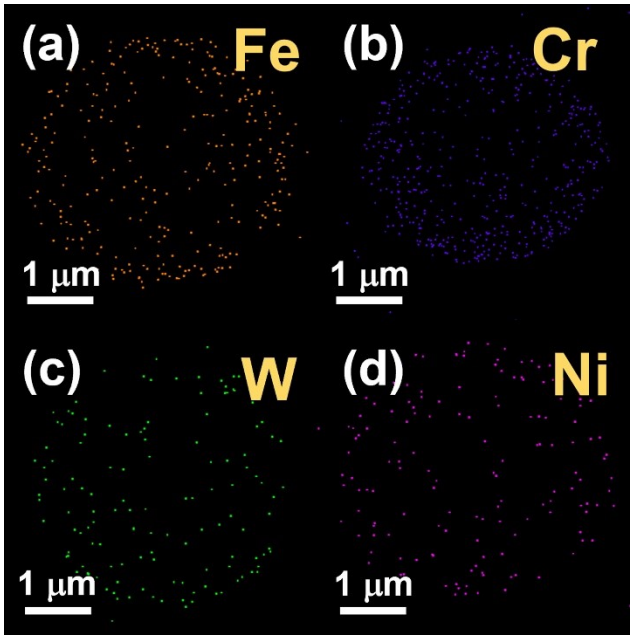

Fig. S3 Mapping images of various dopants in H-CoS-C-CNT.

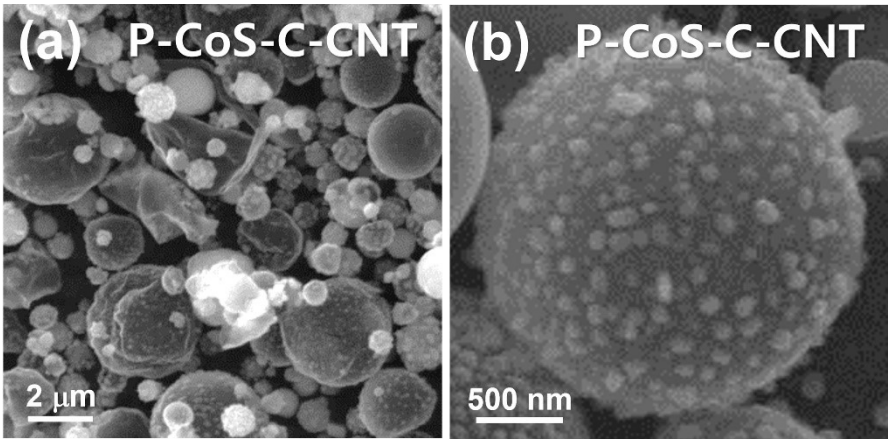

Fig. S4 SEM images of P-CoS-C-CNT microspheres.

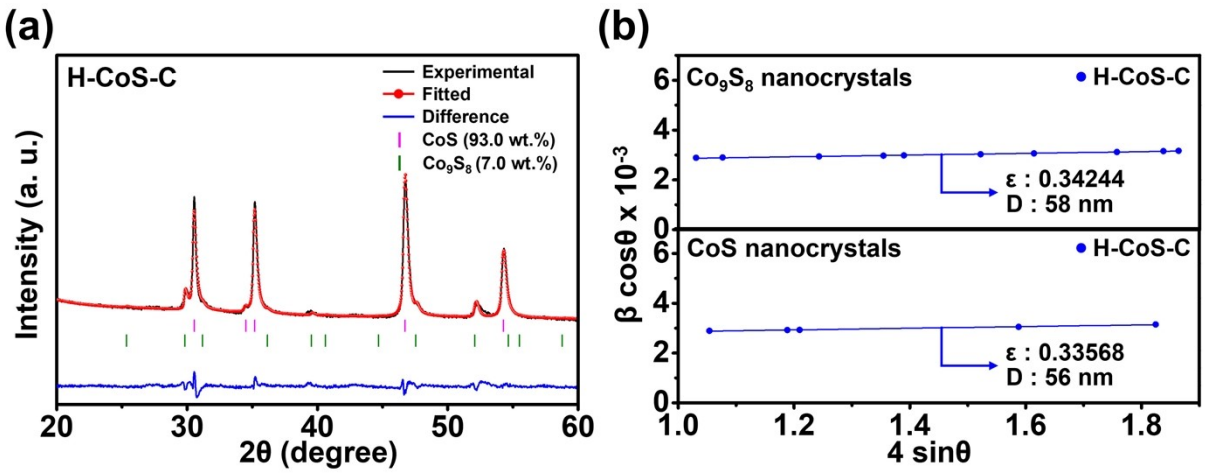

Fig. S5 (a) Rietveld refined XRD pattern for H-CoS-C and (b) Williamson-Hall plots of H-CoS-C for Co_9S_8 and CoS nanocrystals.

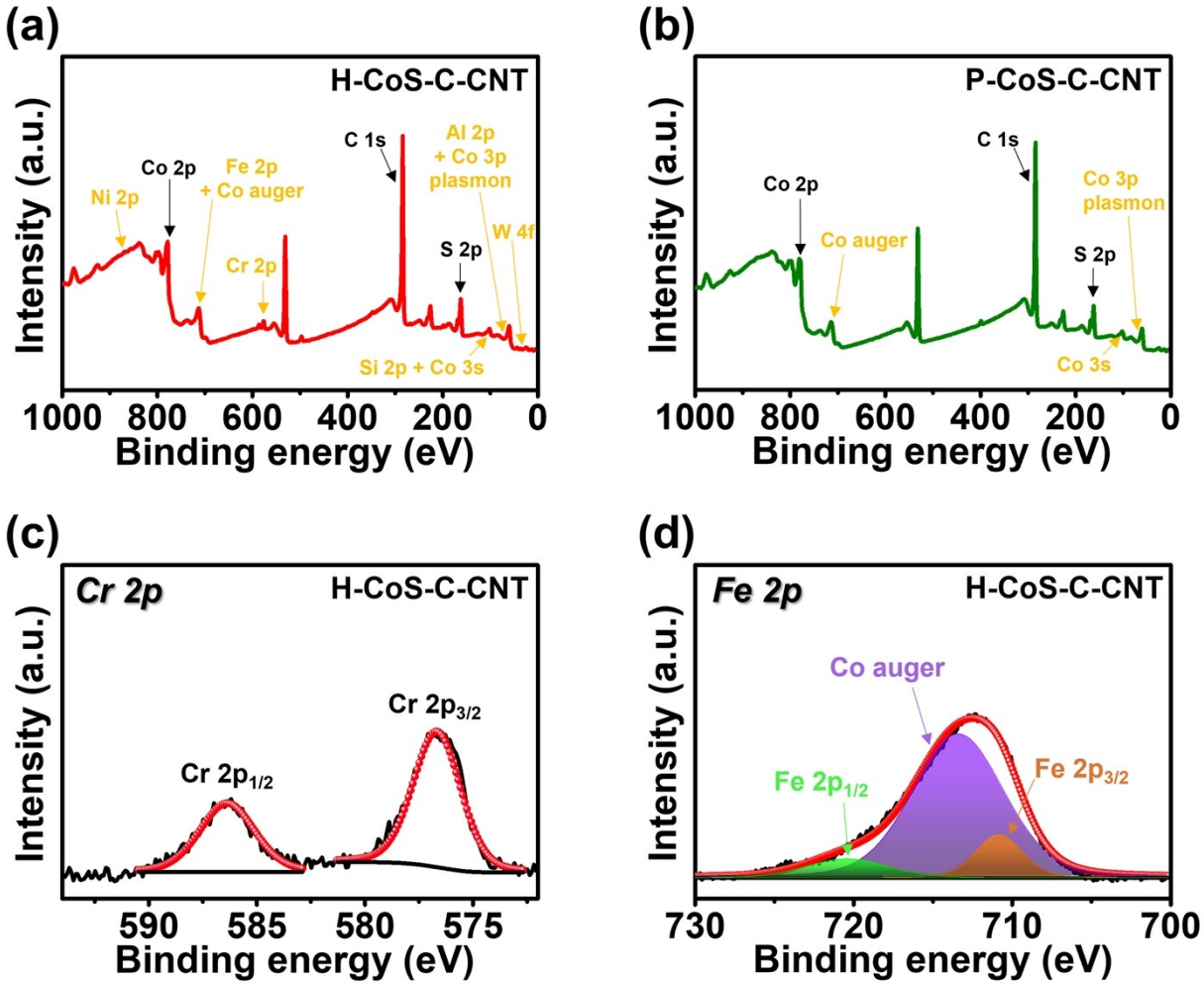

Fig. S6 Wide-scan XPS spectra of (a) H-CoS-C-CNT and (b) P-CoS-C-CNT. High resolution XPS spectra of (c) Cr 2p and (d) Fe 2p for H-CoS-C-CNT.

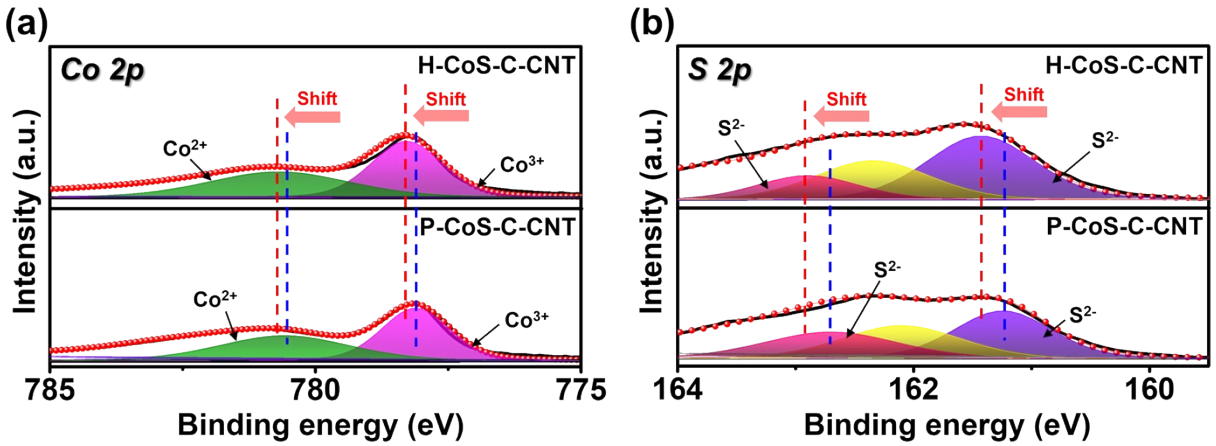

Fig. S7 Magnified XPS spectra of H-CoS-C-CNT and P-CoS-C-CNT corresponding to (a) Co 2p and (b) S 2p regions.

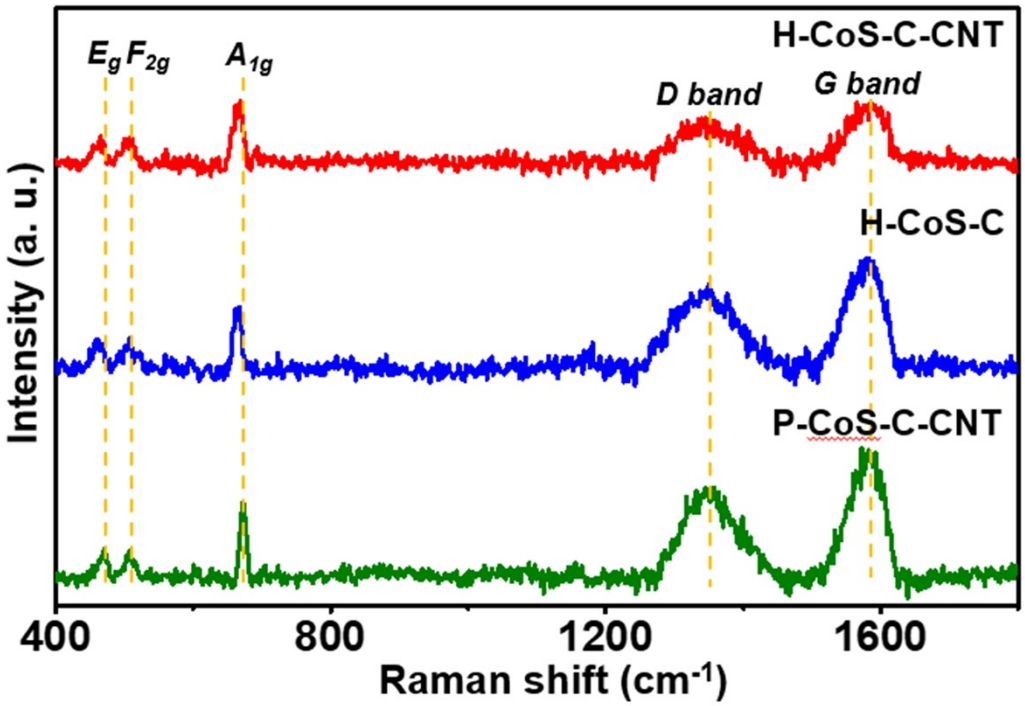

Fig. S8 Raman spectra of H-CoS-C-CNT, H-CoS-C, and P-CoS-C-CNT.

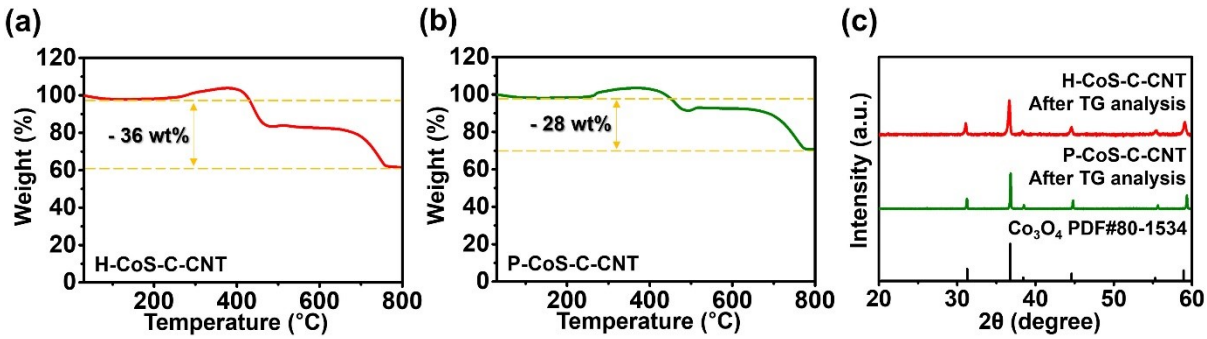

Fig. S9 TG curves of (a) H-CoS-C-CNT, (b) P-CoS-C-CNT, and XRD patterns of these samples after TG analysis.

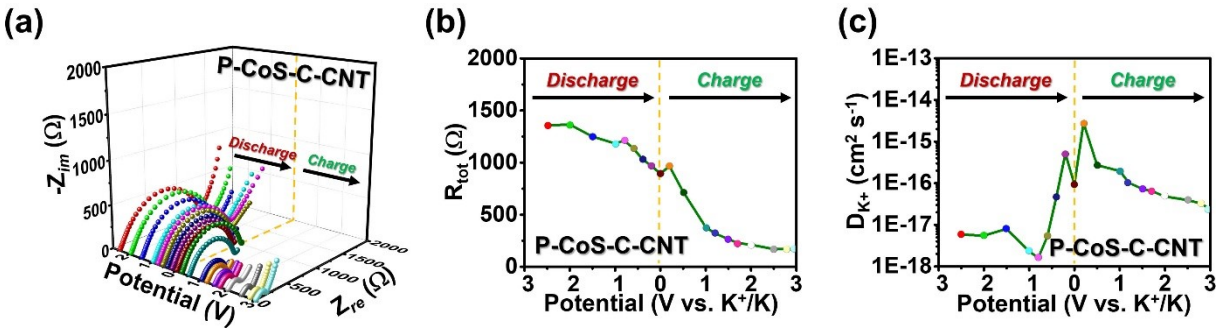

Fig. S10 (a) In-situ EIS Nyquist plots of P-CoS-C-CNT in the initial cycle, (b) variation in resistance values, and (c) variation in potassium-ion diffusion coefficients calculated from in-situ EIS data.

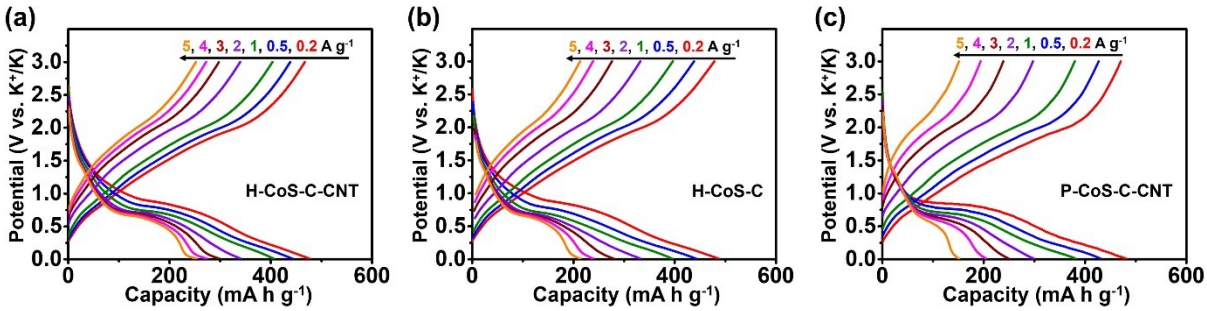

Fig. S11 Galvanostatic discharge/charge potential profiles during the rate capability tests for the (a) H-CoS-C-CNT, (b) H-CoS-C, and (c) P-CoS-C-CNT electrodes.

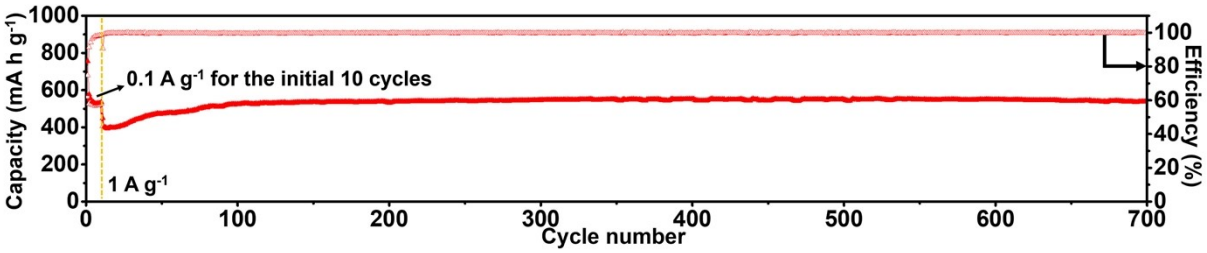

Fig. S12 Long term cycling performance of H-CoS-C-CNT at current densities of 1 A g^{-1}, initially activated at a current density of 0.1 A g^{-1} for ten cycles.

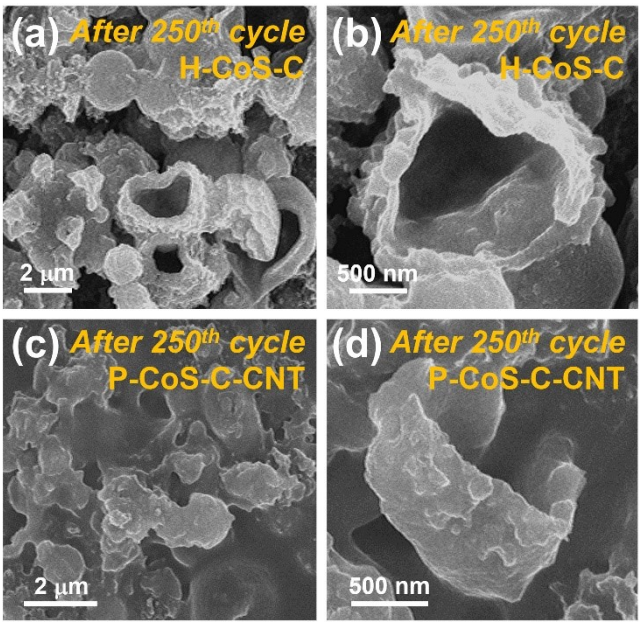

Fig. S13 SEM images of (a and b) H-CoS-C and (c and d) P-CoS-C-CNT electrodes after 250 cycles.

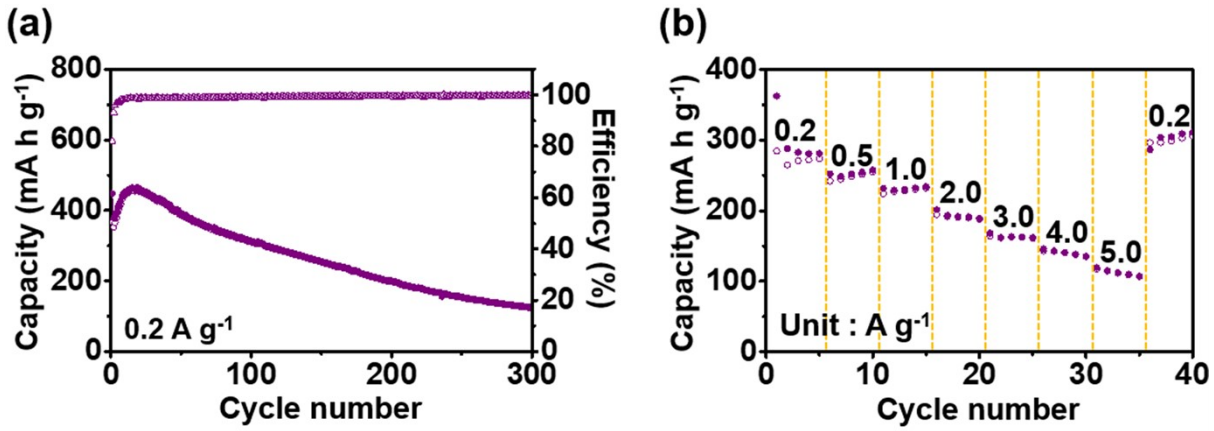

Fig. S14 Electrochemical performances of H-CoS/CoO-C: (a) cycle performance at a current density of 0.2 A g^{-1} and (b) rate performance.

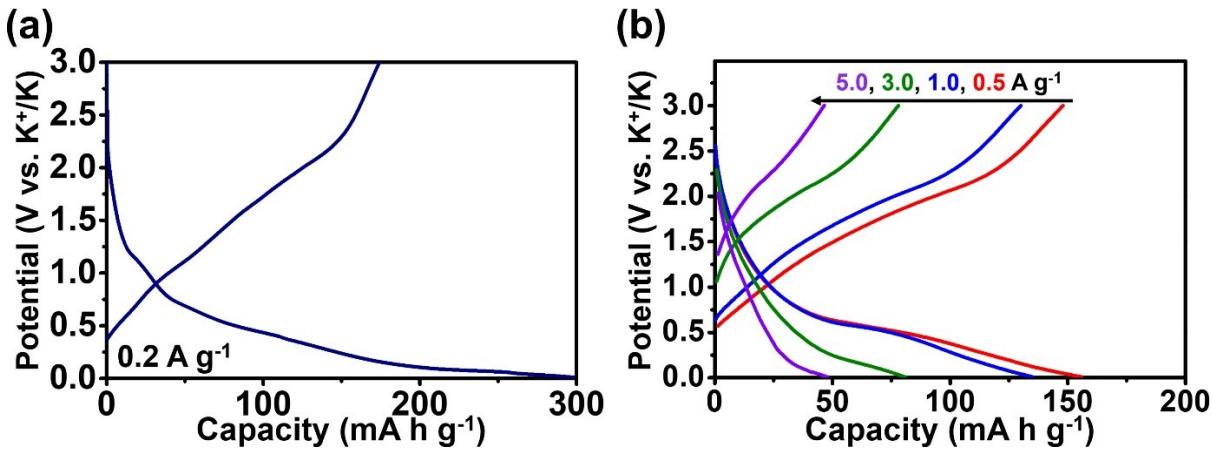

Fig. S15 Electrochemical performances of H-CoO: (a) initial discharge/charge potential profiles at a current density of 0.2 A g^{-1} and (b) discharge/charge profiles at various current densities.

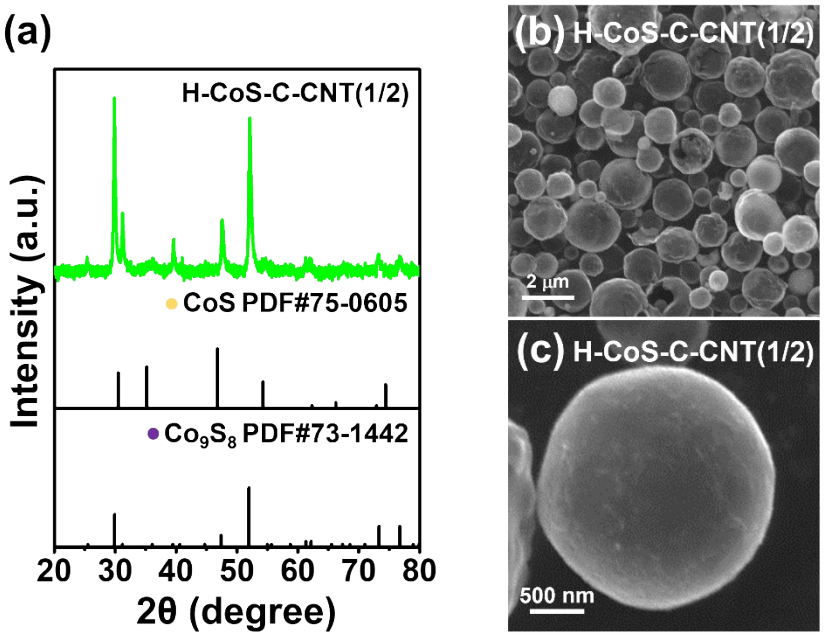

Fig. S16 (a) XRD pattern and (b,c) SEM images of H-CoS-C-CNT(1/2).

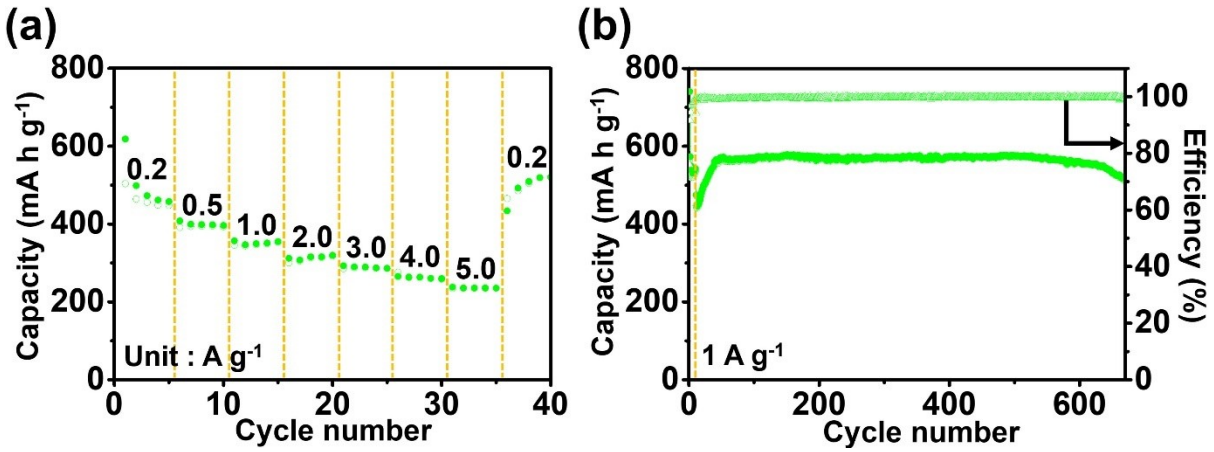

Fig. S17 Electrochemical performances of H-CoS-C-CNT(1/2): (a) rate performance and (b) long term cycling performance at a current density of 1 A g^{-1}, initially activated at a current density of 0.1 A g^{-1} for ten cycles.

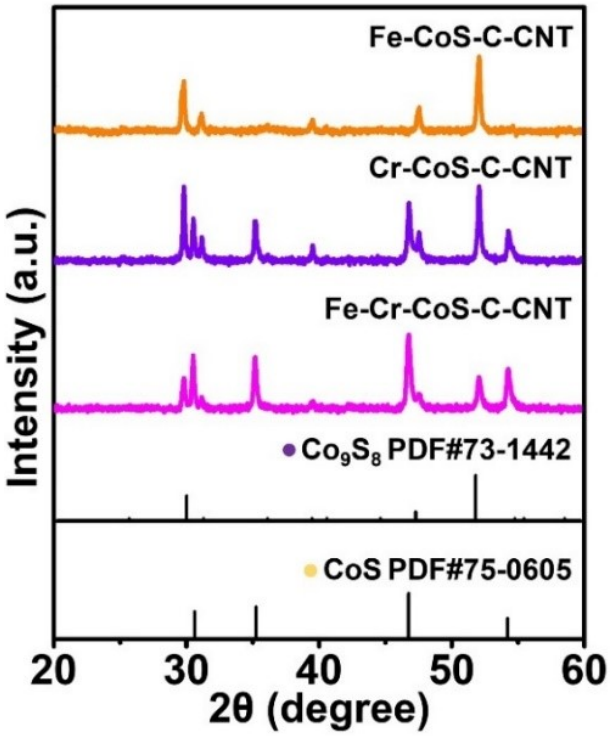

Fig. S18 XRD patterns of Fe-CoS-C-CNT, Cr-CoS-C-CNT, and Fe-Cr-CoS-C-CNT samples.

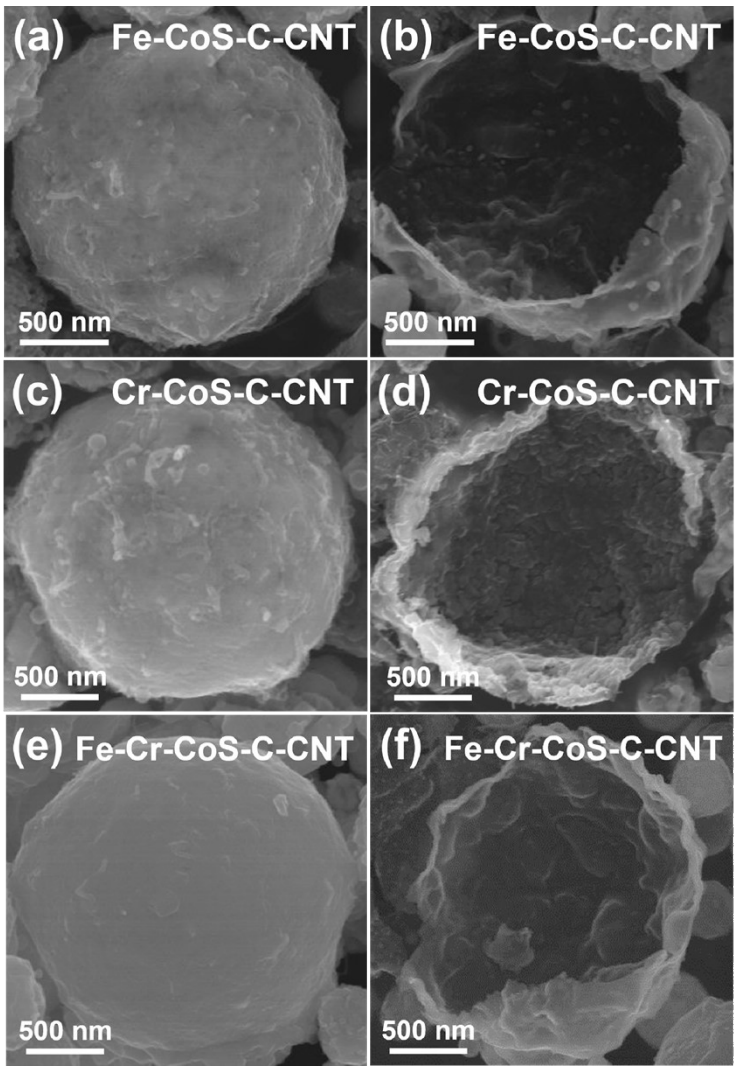

Fig. S19 SEM images of (a,b) Fe-CoS-C-CNT, (c,d) Cr-CoS-C-CNT, and (e,f) Fe-Cr-CoS-C-CNT samples.

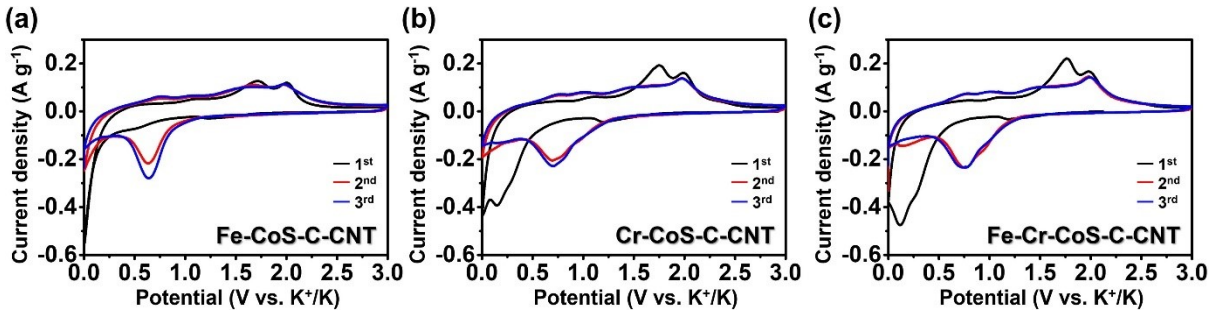

Fig. S20 CV curves at a scan rate of 0.1 mV s^{-1} for (a) Fe-CoS-C-CNT, (b) Cr-CoS-C-CNT, and (c) Fe-Cr-CoS-C-CNT.

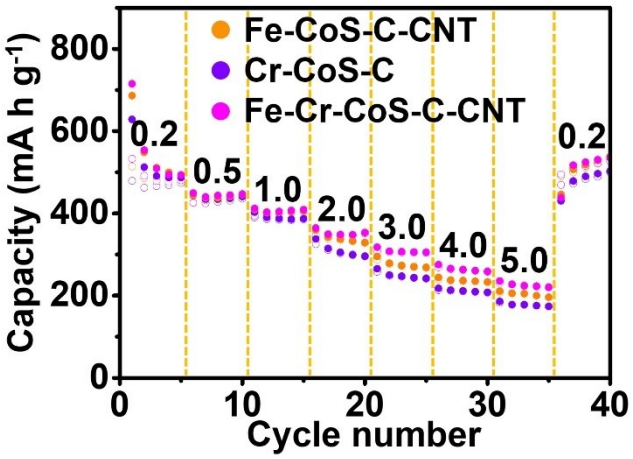

Fig. S21 Rate performances for Fe-CoS-C-CNT, Cr-CoS-C-CNT, and Fe-Cr-CoS-C-CNT.

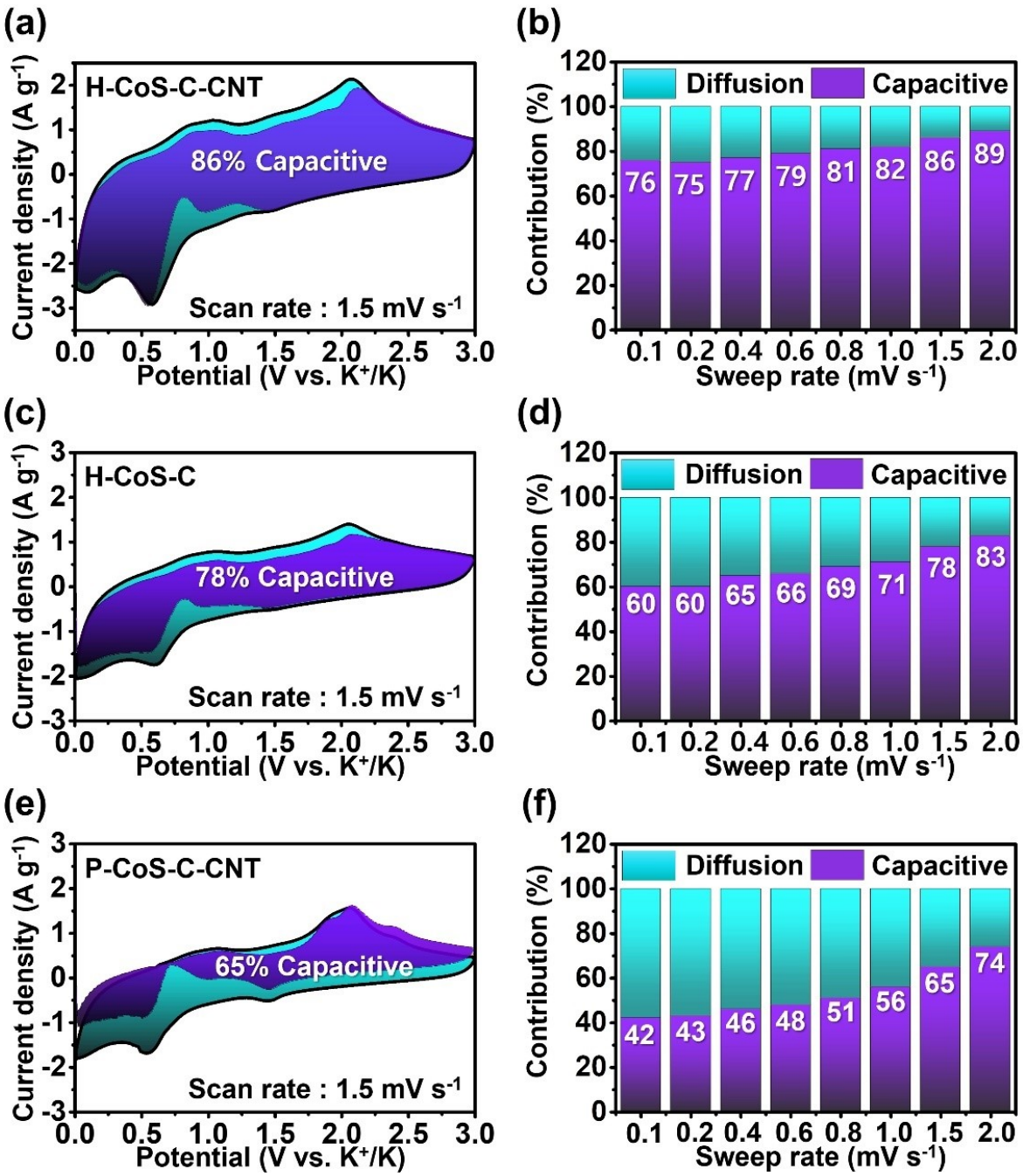

Fig. S22 CV curves showing capacitive contribution (violet colored area) to the total current for (a) H-CoS-C-CNT, (c) H-CoS-C, and (e) P-CoS-C-CNT, and capacity contribution at different scan rates for (b) H-CoS-C-CNT, (d) H-CoS-C, and (f) P-CoS-C-CNT.

Table. S1 Crystallite sizes and lattice strains of H-CoS-C-CNT, H-CoS-C, and P-CoS-C

Sample ID		D (nm)	ε
Co_9S_8 nanocrystals	H-CoS-C-CNT	34	-0.05817
	H-CoS-C	58	0.34244
	P-CoS-C-CNT	82	0.97498
CoS nanocrystals	H-CoS-C-CNT	33	-0.05522
	H-CoS-C	56	0.33568
	P-CoS-C-CNT	82	0.96884

Table. S2 Inductive coupled plasma (ICP) data of H-CoS-CNT and P-CoS-C-CNT samples.

Sample ID		H-CoS-C-CNT	P-CoS-C-CNT
concentration (mol%)	Co	43.78	47.45
	S	51.89	52.55
	Ni	0.30	
	Fe	1.99	
	W	0.15	
	Si	0.07	
	Al	0.13	
	Cr	1.69	

Table S3. Elemental analysis result of H-CoS-C-CNT and P-CoS-C-CNT.

Sample	Carbon (wt%)	Sulfur (wt%)
H-CoS-C-CNT	19.0	23.1
P-CoS-C-CNT	19.1	22.3

Table. S4 ICP data of Fe-CoS-C-CNT, Cr-CoS-C-CNT, and Fe-Cr-CoS-C-CNT samples.

Sample ID		Fe-CoS-C-CNT	Cr-CoS-C-CNT	Fe-Cr-CoS-C-CNT
concentration (mol%)	Co	50.81	47.51	46.40
	S	47.25	50.97	50.24
	Fe	1.94		1.87
	Cr		1.52	1.49